Received: 28 June 2023 | Revised: 9 August 2023 | Accepted: 15 August 2023

DOI: 10.1002/nano.202300097

RESEARCH ARTICLE

Nano Select Open Access WILEY

Semi-solid 3D printing of mesoporous silica nanoparticle-incorporated xeno-free nanomaterial hydrogels for protein delivery

Alaa Mahran[1,2] | **Ezgi Özliseli**[1] | **Qingbo Wang**[3] | **Ilayda Özliseli**[1] | **Rajendra Bhadane**[1,4] | **Chunlin Xu**[3] | **Xiaoju Wang**[1,3] | **Jessica M. Rosenholm**[1]

[1]Pharmaceutical Sciences Laboratory, Faculty of Science and Engineering, Åbo Akademi University, Turku, Finland

[2]Department of Pharmaceutics, Faculty of Pharmacy, Assiut University, Assiut, Egypt

[3]Laboratory of Natural Materials Technology, Faculty of Science and Engineering, Åbo Akademi University, Turku, Finland

[4]Institute of Biomedicine, Research Unit for Infection and Immunity, University of Turku, Turku, Finland

Correspondence
Jessica M. Rosenholm, Pharmaceutical Sciences Laboratory, Faculty of Science and Engineering, Åbo Akademi University, Turku, 20520, Finland.
Email: jessica.rosenholm@abo.fi

Funding information
Sigrid Juséliuksen Säätiö; Magnus Ehrnroothin Säätiö; Svenska Kulturfonden; Academy of Finland, Grant/Award Number: 333158; Higher Education of the Arab Republic of Egypt; Varsinais-Suomen Rahasto, Grant/Award Number: A77805

Abstract

Multifunctional biomaterial inks are in high demand for adapting hydrogels in biomedical applications through three-dimensional (3D) printing. Our previously developed xeno-free system consisting of anionic cellulose nanofibers (T-CNF) and methacrylated galactoglucomannan (GGMMA) as a photo(bio)polymer provides high-performance ink fidelity in extrusion-based 3D printing. The fusion between nanoparticles and this biomaterial-ink system is a promising yet challenging avenue worth exploring, due to the colloidal stability of T-CNF being sensitive to electrostatic interactions. Mesoporous silica nanoparticles (MSNs), with their robust ceramic matrix and fine-tunable surface chemistries, are well-established nanocarriers for different biologicals. Here, we fabricated MSNs with different surface modifications resulting in a net surface charge ranging from highly negative to highly positive to develop printable MSNs-laden nanocomposite biomaterial inks. We utilized rheology as a comprehensive tool to address the matrix interactions with differently surface-charged MSNs. Fluorescently labeled bovine serum albumin (FITC-BSA) was used as a model protein for MSN loading, whereby negatively or neutral-charged MSNs were found suitable to formulate FITC-BSA-loaded biomaterial inks of T-CNF/GGMMA. Depending on the particles' surface charge, FITC-BSA showed different release profiles and preserved its stability after release. Lastly, the proof-of-concept to deliver large-sized biological cargo with MSN-laden nanocomposite biomaterial inks was established via the 3D printing technique.

KEYWORDS
cellulose nanofibers, hydrogel extrusion 3D printing, mesoporous silica nanoparticles, methacrylated galactoglucomannan, nanocomposite biomaterial

1 | INTRODUCTION

Hydrogel-based three-dimensional (3D) printing has received considerable interest in various biomedical sections such as tissue engineering, regenerative medicine, wound healing, and personalized medicine.[1–4] Fabricating scaffolds specific to each patient with defined properties and high precision is advantageous in therapeutics, with increasing attention being paid towards more personalized solutions.[5] These scaffolds would not only provide early disease diagnosis tools through in vitro disease modeling but also treatment customization and accurate dosing with appropriate release profiles, which can be achieved in efficient and targeted ways to meet an individual's needs.[6]

Extrusion-based 3D printing is the most established technique to create 3D hydrogel scaffolds with complex geometries.[7] When using this method, the biomaterial ink should meet specific rheological requirements during printing, as well as maintain a stable structure after printing. Although different polymers could be used as biomaterial inks, natural polymers, especially from plant sources, are gaining more attraction in biomedical applications as they are renewable, biocompatible, and less immunogenic compared to others. [8]

Cellulose nanofibers (CNF) have been recognized as a generic biomaterial, which is applicable as an accommodating matrix for 3D cell culture as well as hydrogel fabrication, ascribed to their 1D nanomorphology mimicking the extracellular matrix.[9] In a hydrogel form, the fibril-fibril network of CNFs endows a porous microstructure enabling the delivery of biologicals and biochemical signals to cells.[10,11] Moreover, CNF has proven to be biocompatible in supporting cell growth and proliferation.[9,12] TEMPO-mediated oxidation of CNF (T-CNF) results in stable hydrogels even at very low concentrations (< 1 wt%).[13] This is attributed to the electrostatic repulsion between negatively charged carboxylate groups on the nanofibril surface, alongside with the extensive fibril-fibril entanglement. Using CNF in hydrogel printing usually needs auxiliary polymers such as alginate or gelatin to improve its printability and printing fidelity.[14,15] Methacrylated galactoglucomannan (GGMMA) is a semi-synthetic derivative of the wood-derived, water-soluble heteropolysaccharides of galactoglucomannan with methacryloyl groups. GGMMA can be photocrosslinked through free radical polymerization of double bonds in its molecular structure, and it has been applied as an alternative to golden standard gelatin methacrylate when formulating xeno-free biomedical hydrogels.[16] In our previous studies, a homogenous biomaterial ink composed of photopolymer GGMMA and T-CNF was successfully 3D printed with high resolution.[16,17] Increasing the functionality of this xeno-free biomaterial system would provide great significance in establishing a hydrogel-based delivery system. Here, the nanocomposite approach is effective with possibilities for integrating functionalities, For example, bioactivity and mechanical characteristics as demanded in a specific biomedical application.[18,19] Incorporation of nanoparticles within the hydrogel matrix can reinforce different polymeric matrices and include multiple functionalities such as controlled release of loaded cargo.[20] Nevertheless, the colloidal stability of anionic T-CNF is sensitive to charged surfaces, which demands fine-tuning upon incorporation of biological agents or nanoparticles into such matrices.[21]

Different nanomaterials have been studied to fabricate nanocomposite hydrogels, such as carbon-based nanoparticles, silica nanoparticles, polymeric nanoparticles, and metallic nanoparticles.[22] Among them, mesoporous silica nanoparticles (MSNs) stand out as they offer tailorable characteristics, large pore volume, and high specific surface area.[23–25] Additionally, MSNs are easily labeled with molecular imaging agents such as fluorescent dyes, which facilitates their detection with different imaging techniques. The presence of free silanol groups on MSNs provides accessible points that can be further functionalized. In our previous study, different MSN surface modifications were investigated for their surface-charge dependent cellular uptake efficiency including cationic amine groups, anionic carboxylic acid groups, and acetyl groups without charge.[26] Surface modification of MSNs can facilitate high loading efficiency and controlled release of different biologicals according to their isoelectric point (IEP).[27–32] As reported by Tu, Boyle et al., positively and negatively charged MSNs were successfully used for loading and delivering different proteins with different IEP (both negative and positive) depending on the electrostatic interactions between the MSNs and proteins.[33] Recent studies with MSN-based nanocomposite hydrogels have reported improved bioactivity and mechanical properties of the hydrogel imparted by the incorporation of the nanoparticles.[34–36] 3D printing of MSN-incorporated nanocomposite biomaterials was previously developed using gelatin methacrylate (GelMA) as a polymeric matrix and MSNs, post-synthesis functionalized with calcium, phosphate, and dexamethasone, as inorganic components for bone tissue repair and regeneration.[37] Cationic silica nanoparticles were reported to reinforce anionic polymers and improve their mechanical properties, printability, and ink fidelity through electrostatic interactions.[38]

In our study, we hypothesized that the surface chemistry of T-CNF can be affected by differently surface-charged

MSNs, which can affect the stability and printability of the developed ink as well as drug release out of the printed structure. Therefore, we aimed to develop xeno-free mesoporous silica nanocomposite biomaterial inks with good printability and suitable mechanical stability for the delivery of different biologicals. To date, very few studies are available to unravel the mechanisms of the protein-MSN, MSN-hydrogel, and protein-MSN-hydrogel interactions to formulate 3D printable nanocomposite inks.[39–41] Herein, large pore size (10 nm) MSNs were synthesized as suitable vehicles for protein delivery, and the nanoparticle surface was further modified to achieve positively charged amino groups (PEI-MSNs), negatively charged carboxylic acid groups (SUC-MSNs) and acetyl groups with neutral charge (ACA-MSNs). When FITC-BSA was used as a model protein, the loading capacities of nanoparticles showed variation depending on their surface charge properties. Rheology was used as a comprehensive tool to study the matrix interaction with different surface-charged MSNs before and after protein loading. Printability and in vitro release of the protein-loaded biomaterial inks were assessed. Moreover, nano differential scanning fluorimetry (NanoDSF) was used to confirm the protein stability after MSNs loading and 3D printing. [42] The as-developed nanocomposite systems present a promising drug delivery platform for biologicals and biochemical components such as growth factors and enzymes that can regulate several cellular processes, potentially for a wide spectrum of applications in tissue engineering and personalized medicine realized via additive manufacturing.

2 | MATERIALS

Cetyltrimethylammonium chloride (CTAC) solution (25 wt% in H_2O), tetraethyl orthosilicate (TEOS, 98%), triethylamine (TEA, ≥99%), (3-Aminopropyl)triethoxysilane (APTEs, 99%), ammonium nitrate, glacial acetic acid, sodium acetate, 4-(2-hydroxyethyl)−1-piperazineethanesulfonic acid buffer (HEPES), succinic anhydride (≥99%), acetic anhydride (≥99%), fluorescein isocyanate (FITC, ≥90%) and tetramethylrhodamine isocyanate (TRITC), anhydrous toluene (99.8%), cyclohexane (99.5%), bovine serum albumin (BSA) and lithium phenyl-2,4,6-trimethylbenzoylphosphinate (LAP, ≥95%) were purchased from Sigma Aldrich. Aziridine (98%) was obtained from Menadiona, Spain. TEMPO-oxidized cellulose nanofibers (T-CNF) and methacrylated galactoglucomannan (GGMMA) were in-house synthesized and the detailed protocol can be found in the supplementary information. Bradford dye reagent (Coomassie brilliant blue G-250 dye) was obtained from Bio-Rad laboratories and measurements were carried out according to manufacturers' instructions. Double-distilled Milli-Q water was used throughout the work. All chemicals are used as received.

3 | METHODS

3.1 | Preparation of non-labeled and tetramethylrhodamine isocyanate (TRITC)-labeled mesoporous silica nanoparticles (MSNs)

The non-labeled 10 nm pore-sized MSNs were synthesized according to the procedure of Shen et al. [43] In a 100 mL round bottom flask, water (36 mL), CTAC (24 mL), and TEA (0.18 g) were placed and stirred in an oil bath at 60°C. After 1 hour of stirring, (20 mL) TEOS solution in cyclohexane (20 v/v%) was slowly added and kept at 60°C for 24 hours. Then, the particles were collected by centrifugation of the reaction mixture at 18000 rpm for 20 minutes at 10°C. After discarding the supernatant, the particles were washed two times with absolute ethanol using the same settings. Surfactant in the pores was extracted using the ion exchange method with ethanolic ammonium nitrate solution (0.6 wt%) by stirring at 60°C for 6 hours and centrifugation to collect, and the procedure was repeated twice. Finally, the particles were washed with ethanol two times and kept in ethanol for further use.

Fluorescently labeled nanoparticles (TRITC-labeled MSNs) were prepared by co-condensation functionalization, which means incorporating amine-reactive fluorescent dye during the synthesis. The amine-reactive dye solution was prepared by dissolving TRITC (1.5 mg) in absolute ethanol (1 mL) followed by the addition of APTES (0.02 mL) and stirring for 2 hours under an inert atmosphere.[44]

3.2 | Surface modification of MSNs

The surface silanol groups of prepared MSNs were post-synthesis grafted with polyethylene imine through hyperbranched surface polymerization of aziridine to yield PEI-MSNs. Surface polymerization was carried out by dispersing the nanoparticles (100 mg) in toluene (10 mL) followed by adding acetic acid (0.0052 mL) as a catalyst and aziridine (0.052 mL). The reaction was refluxed overnight, and the prepared particles were washed two times with ethanol through separation via centrifugation in between (18000 rpm, 20 minutes).[45]

Subsequently, the primary amino groups of PEI-MSNs were further modified with succinic anhydride (succinylation) and acetic anhydride (acetylation) to yield negatively

charged succinic acid groups (SUC-MSNs) and uncharged acetyl groups (ACA-MSNs), respectively. For each, PEI-MSNs particles (50 mg) were dispersed in ethanol (50 mL). Then, SUC-MSNs were prepared by adding (4 mL) of succinic anhydride solution in ethanol (5 mg mL^{-1}).[46] For ACA-MSNs, acetic anhydride (0.4 mL) was added to PEI-MSNs particles.[26]The reactions were left overnight, and the prepared particles were washed with ethanol two times to remove unreacted chemicals.

3.3 | Characterization of the MSNs

The hydrodynamic diameter and net surface charge of the prepared nanoparticles were determined through dynamic light scattering (DLS) and ζ-potential measurements by using Malvern ZetaSizer NanoZS (Malvern Instruments Ltd., Worcestershire, UK). For DLS measurements, the particles were diluted with ultrapure water to make a final concentration of 0.2 mg mL^{-1}. ζ-potential measurements were carried out in different buffers of different pH. Non-labeled, TRITC-labeled, and protein-loaded MSNs were dispersed in HEPES buffer (25 mM, pH 7.2) with a concentration of 0.2 mg mL^{-1} to validate the successful surface functionalization and final net surface charge of MSNs after protein loading. ζ-potential of non-labeled MSNs was measured in acetic acid/sodium acetate buffer at pH 4, 5, and 6 (25 mM) to determine suitable pH for protein loading.

The morphological structure of the pristine MSNs was observed using transmission electron microscopy (TEM) (JEM 1400-Plus, JEOL Ltd., Tokyo, Japan). The particles were dispersed in ethanol and dropped onto a carbon-coated copper TEM grid and left for drying before measurements.[47]

3.4 | Protein labeling and loading

BSA labeling with fluorescein isocyanate (FITC) was prepared by dissolving BSA (200 mg) in sodium bicarbonate solution (100 mL) (0.1 M, pH 9). Then, (5 mL) FITC solution in DMSO (1 mg mL^{-1}) was slowly added to the BSA solution and left stirring overnight at 4°C. The following day, the FITC-BSA solution was dialyzed using a dialysis membrane with 3500 molecular weight cut-off (MWCO) for 48 hours against ultrapure water and the resulting FITC-BSA was freeze-dried and stored at 4°C until further use.

FITC-BSA loading was carried out at different pH to find the suitable pH condition for protein loading. FITC-BSA was loaded into non-labeled nanoparticles (MSNs, PEI-MSNs, ACA-MSNs, and SUC-MSNs) using acetic acid/sodium acetate buffer (25 mM) at pH 4, 5, and 6 through mixing for 5 hours at room temperature using protein: MSN weight ratio of 1:2.[48] Then, to find the optimum weight ratio for protein loading, non-labeled nanoparticles were loaded with FITC-BSA in acetate buffer (25 mM, pH 5) in three different protein:MSN weight ratios 1:2, 1:1, and 2:1 using the same loading procedure. In all loading trials, nanoparticles concentration in acetate buffer was kept constant (2 mg mL^{-1}). After each trial, the supernatant was taken after centrifugation at 13000 rpm for 15 minutes and free unloaded protein was measured using UV-Vis Spectrophotometer (Nanodrop 2000c, Thermo Fisher Scientific, Wilmington, NC, USA) at wavelength 280 nm. Loading capacity and entrapment efficiency were calculated for each trial as shown in Equation 1 and 2[33]

$$\text{Loading capacity}\% = \frac{\text{PT} - \text{PF}}{\text{NT}} \quad (1)$$

$$\text{Entrapment efficiency}\% = \frac{\text{PT} - \text{PF}}{\text{PT}} \quad (2)$$

where P_T is the total protein amount, P_F is the free unloaded protein amount, N_T is the total NPs amount.

TABLE 1 Composition of nanocomposite hydrogel.

Formulation	T-CNF wt%	GGMMA wt%	LAP wt%	MSN[a] wt%
F_0	1	2	0.2	–
$F_{0.5}$	1	2	0.2	0.5
F_1	1	2	0.2	1
$F_{2.5}$	1	2	0.2	2.5

Abbreviations: GGMMA, methacrylated galactoglucomannan; LAP, lithium phenyl-2,4,6-trimethylbenzoylphosphinate; MSN, Mesoporous silica nanoparticles; T-CNF, anionic cellulose nanofibers;
[a]MSN: MSNs, PEI-MSNs, ACA-MSNs, and SUC-MSNs.

3.5 | Nanocomposite-hydrogel formulation

Nanocomposite hydrogel was formulated using T-CNF as a hydrogel matrix, GGMMA as a photo-curable agent, LAP as a photoinitiator, and MSNs as nanocarriers. Due to LAP sensitivity to light, it is covered with aluminum foil in all the experiments. The composition of nanocomposite hydrogels in detail is listed in Table 1. The concentration of T-CNF, GGMMA, and LAP was kept constant in all formulations with changing nanoparticle concentrations, and 1 g of hydrogel was prepared for each experiment. First, T-CNF was combined with lyophilized powder GGMMA and LAP at 50°C using a vortex mixer until GGMMA and LAP were completely dissolved to produce homogenous hydrogel. Then, the corresponding amount of the nanoparticles

was physically incorporated into the hydrogel matrix until it became homogenously distributed.

3.6 | Rheological assessments of MSN-laden hydrogel

The rheological properties were assessed for the plain hydrogel and non-loaded nanocomposite hydrogels (MSNs, PEI-MSNS, ACA-MSNs, and SUC-MSNs) in three different concentrations (0.5, 1, and 2.5 wt%). Additionally, FITC-BSA-loaded hydrogel (0.5 wt%) and FITC-BSA-loaded nanocomposite hydrogels (MSNs, PEI-MSNs, ACA-MSNs, and SUC-MSNs) using 1 wt% nanoparticles were evaluated to characterize protein-loaded hydrogels. All the measurements were carried out using the HAAKE MARS Modular Advanced Rheometer system (Thermo-Scientific, Karlsruhe, Germany) with a cone-plate geometry measuring system (diameter 20 mm, 1° cone angle with a truncation gap 0.049 mm) and the temperature was set at 23°C. All samples before each measurement were equilibrated at a shear rate of 0 s^{-1} for 60 s.

The flow behavior of different formulations was determined through shear rate ramp-up 0.01-1000 s^{-1} in logarithmic scale with 1 second per data point. The power law index and consistency index were calculated using the power law equation (Equation 3).[15]

$$\eta = K\gamma^{n-1} \tag{3}$$

where η is the dynamic viscosity is the shear rate, K is the consistency index, and n is the power law index or flow behavior index.

The viscoelastic properties were probed through amplitude sweep and oscillatory time sweep tests. The amplitude sweep test was carried out by applying a shear strain from 0.0% to 10% at a constant frequency of 1.6 Hz with a data acquisition time of 10 s per data point. The thixotropic behavior of the tested formulations was evaluated using oscillatory time sweep test by straining the sample first 0.02% for 60 s then straining 10% for 10 s followed by straining 0.02% for 60 s at a constant frequency of 1.6 Hz.

From the amplitude sweep test, linear viscoelastic region (LVER), which describes the region of elasticity and linearity between shear strain and shear stress, was determined by the value of shear strain at which shear stress deviates from linearity by 10%. Gel strength was measured as the storage modulus value (G') at the end of LVER. Finally, the flow transition index (FTI) was calculated using Equation 4

$$\mathrm{FTI} = \frac{\tau_f}{\tau_y} \tag{4}$$

in which τ_f is the flow stress and obtained from the shear stress value at the crossover point between storage modulus (G') and loss modulus (G") and τ_y is the yield stress, which is the shear stress value at the end of the LVER.

3.7 | Semi-solid 3D printing

The printability of different biomaterial inks (plain hydrogel and 1 wt% FITC-BSA-loaded nanocomposite hydrogels (MSNs, PEI-MSNs, ACA-MSNs, and SUC-MSNs)) were evaluated using extrusion-based 3D printing (Brinter One, Brinter Ltd., Finland). Stainless steel needles (Nordson EFD, USA) with a small inner diameter of 0.25 mm were used for the plain hydrogel, whereas a larger inner diameter (0.33 mm) was used for printing nanocomposite inks to prevent repeated nozzle clogging due to the nanoparticles. A pneumatic tool cooled printhead with the temperature set at 20°C and the temperature of the print bed at 16°C was used throughout the study. A two-layered grid construct was used for optimization, different printing speed ranging between 8 to 12 mm s^{-1} and the pressure ranging from 250 to 400 mbar were screened to determine the most suitable parameters for each ink. Photo-crosslinking was done using UV/Vis LED module with wavelength 405 nm and intensity 17.5 mW cm^{-2} for 30 seconds after each layer and 60 seconds for the post-curing process. The printability index (Pr) of the printed constructs was determined using optical microscopic images of EVOS microscope (AMG, Mill Creek, Washington) and ImageJ software (National Institute of Health, Gaithersburg, MD, USA) using Equation 5:

$$\mathrm{Pr} = \frac{\mathrm{L}^2}{16 \times \mathrm{A}} \tag{5}$$

in which L is the perimeter, and A is the experimental area.

3D circular structures (10 × 10 ×1 mm) designed by Autodesk Fusion 360 software were printed as four layered grid structures using the optimal settings and used for in vitro release and microscopy studies.

3.8 | In vitro studies

3.8.1 | In vitro protein release study

In vitro release experiments of protein-loaded nanoparticles and 3D printed protein-loaded nanocomposite structures were conducted using PBS buffer (pH 7.4) as a release media and shaker water bath at 37°C. Protein release from different surface-modified MSNs was determined by dispersing protein-loaded nanoparticles in PBS

buffer to obtain a final concentration of 1 mg mL^{-1} for 72 hours. For 3D printed protein-loaded nanocomposite structures, pre-weighted structures were incubated with 1 mL PBS buffer for 7 days in a 5 mL centrifuge tube. Printed structures of plain and 0.5 wt% FITC-BSA-loaded hydrogels were used as a negative and positive control, respectively. At specified time points (0, 0.25, 0.30, 0.75, 1, 2, 4, 6, 8, 24 hours, and then every 24 hours for 7 days), 0.02 mL samples were taken and replaced with fresh PBS buffer. Short time intervals in the beginning were chosen to detect the protein release profile in the early stage of the release experiments. The protein concentration was determined using Bradford protein assay by diluting release samples with Bradford reagent using a 1:5 ratio and detecting absorbance using UV-Vis Spectrophotometer at wavelength 592 nm. Experiments were conducted in triplicates, and the release kinetics of the different formulations was calculated using the power law equation (Equation 6) introduced by Korsmeyer–Peppas [49] which describes the time-dependent drug fractional release ($\frac{M_t}{M_\infty}$)

$$\frac{M_t}{M_\infty} = k.t^n \tag{6}$$

where Mt and M_∞ are the absolute cumulative amount of drug released at time t and infinite time, respectively; k is the kinetic constant, t is the time, and n is the release power. The exponent n is used to predict the release mechanism when $n \leq 0.45$ corresponds to that drug release is driven by the Fickian mechanism, when $0.5 \leq n \leq 0.8$ is anomalous transport, and when $0.8 \leq n \leq 1$, the mechanism is case II transport.

3.8.2 | Protein thermal stability study

The stability of the protein after release was assessed using NanoTemper Prometheus NT 4.8 (NanoTemper Technologies GmbH, Germany) at different time points (4, 8, 24, and 48 hours). The NanoTemper technology relies on intrinsic tryptophan fluorescence (ITF) measurements at 330 and 350 nm during protein unfolding caused by increasing temperature. The samples from the release media were loaded into high-sensitivity glass capillaries (Cat#PR-C006, NanoTemper Technologies, GmbH, Germany) and heated from 20 to 95°C at a rate of 2°C $minute^{-1}$. FITC-BSA at a concentration of 1 mg mL^{-1} in PBS buffer (pH 7.4) was used as a control. The Therm Control Software V 2.1.5 was utilized to generate a plot of the fluorescence intensity (F350/F330) ratio against the temperature, and the melting temperature (Tm), the temperature at which half of the protein is unfolded, was determined using the inflection point (IP350/330) from the first derivative.[50]

3.8.3 | Evaluation of nanoparticles and protein release by confocal microscopy and transmission electron microscopy

To be able to visualize the localization of nanoparticles within the matrix and confirm the protein release using fluorescence, TRITC-labeled MSNs were used in this study. FITC-BSA-loaded TRITC-labeled MSNs were incorporated into the hydrogel (T-CNF and GGMMA) using the previously described method. 3D printed protein-loaded nanocomposite structures imaged post printing and after the release study by submerging in PBS to eliminate drying during acquisition. Images were acquired using 3i CSU-W1 spinning disk confocal microscopy integrated with Hamamatsu sCMOS Orca Flash4.0 camera with 488 and 561 nm lasers and ASI piezo stage. 10x objective was used to capture 3D volumetric images with the dimension of $650 \times 650 \times 500$ µm, and obtained images were illustrated using Slidebook 6 Software.

Additionally, nanoparticle diffusion from the matrix and degradation were investigated using TEM by collecting samples from the release medium (0.1 mL) during the release study at 24 hours and 7 days timepoint. The collected samples were then centrifuged at 13000 rpm for 10 minutes and the pellet was redispersed with acetone (0.03 mL). The suspension was dropped on a copper carbon grid and left for drying before acquisition by TEM.

4 | RESULTS AND DISCUSSION

4.1 | Physicochemical characterization (hydrodynamic size, PDI, ζ-potential, and TEM imaging)

Synthesized and surface-modified MSNs were characterized to evaluate the hydrodynamic size, size distribution, and colloidal stability in the suspension after surface modification and TRITC labeling processes. Figure 1A shows a schematic representation of MSNs and different surface modifications. The hydrodynamic diameter and polydispersity index (PDI) values of both non-labeled and TRITC-labeled MSNs with different surface modifications are presented in Figure 1B. Incorporating fluorescent dye did not influence the nanoparticle properties, and all MSNs exhibited a hydrodynamic diameter of around 200 nm. The PDI values of all MSNs were less than 0.2, which indicates a narrow size distribution with good dispersity of the prepared MSNs.

Figure 1C shows the ζ-potential values of non-labeled and TRITC-labeled MSNs. Bare MSNs displayed negative net surface charge due to deprotonation of the surface silanol groups in pH 7.2, as described previously.[27] Due

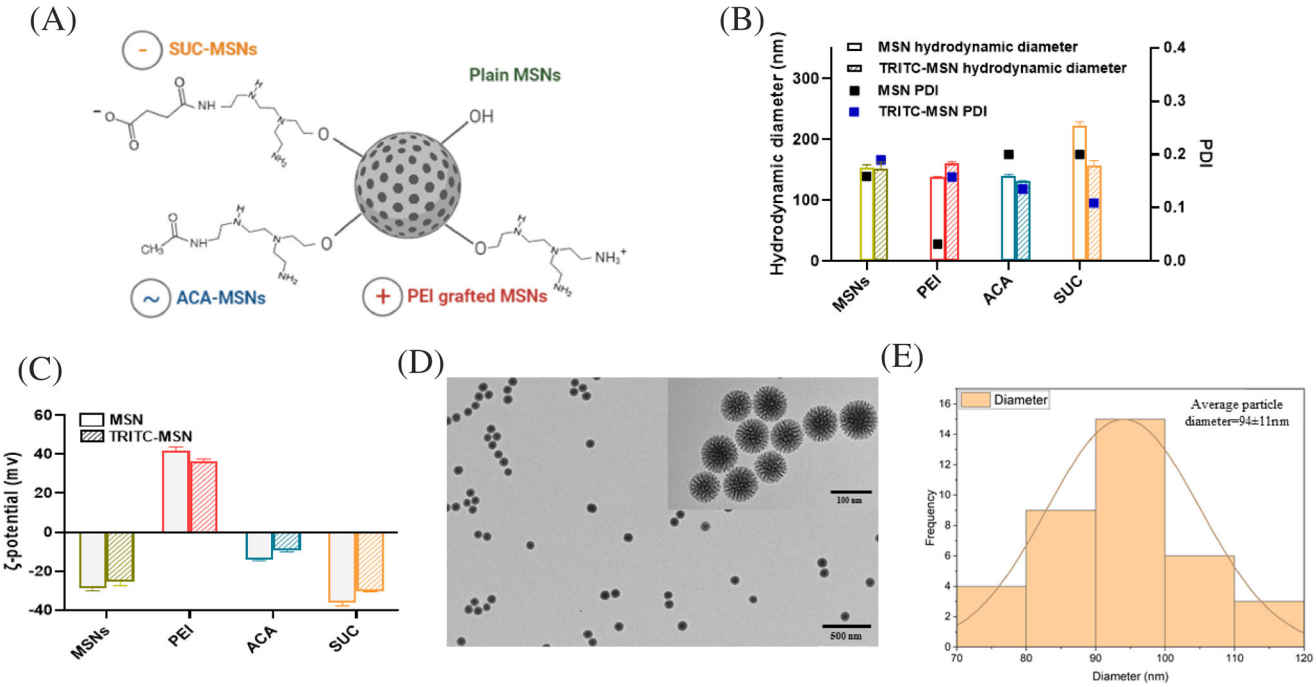

FIGURE 1 Physicochemical characterization of MSNs. (A) Schematic diagram of MSNs and different surface modifications to yield different net surface charge characteristics. (B) The hydrodynamic diameter measurements (Z-average) and PDI of non-labeled MSNs (MSN) and TRITC-labeled MSNs (TRITC-MSN), (C) Zeta potential values of the prepared MSN and TRITC-MSN at neutral pH. Ultrapure water was used for particle size and PDI measurements and HEPES buffer (pH 7.2 (25 mM)) for ζ-potential measurements. (D) TEM images of the fabricated MSNs with a pore size of 10 nm. (E) The particle size distribution histogram of MSNs obtained from three TEM images analysis of 37 particles in total. MSN, Mesoporous silica nanoparticles; PDI, polydispersity index; TRITC, tetramethylrhodamine isocyanate; TEM, transmission electron microscopy.

to the grafting of amino groups onto the surface of MSNs, PEI-MSNs showed a high positive net surface charge indicating successful PEI grafting. Further derivatization of PEI-MSNs with acetic anhydride resulted in MSNs with nearly neutral net surface charge (ACA-MSNs) due to capping of the primary amino groups, where residual amino groups and silanol groups on MSNs surface still contributed to the overall (net) neutral charge. Additionally, highly negatively net surface charged particles SUC-MSNs were obtained by further reaction of primary amino groups on PEI-MSNs with succinic anhydride to yield terminal succinic acid groups. The thus yielded free carboxylate groups on SUC-MSNs provide a zwitterionic coating containing basic or positively charged groups (secondary, tertiary, and any residual primary amines from PEI) and carboxylic acid groups as acidic or negatively charged groups.[26]

TEM images and particle size distribution analysis of the MSNs are depicted in Figure 1D,E, respectively. TEM images show well-dispersed, spherical particles with dendritic center-radial oriented large mesopores with an average particle diameter of 94 ± 11 nm and an average pore size of 9.5 nm.

4.2 | Protein loading optimization

To study protein interactions with differently surface-charged MSNs before and after protein loading, a common protein (FITC-BSA) was used as a model protein. Optimization of protein loading conditions was carried out using different FITC-BSA:MSN weight ratios and buffers of different pH as loading medium. Figure 2A,B shows the percent loading capacity and percent entrapment efficiency of the protein-loaded MSNs in pH 5 at three different weight ratios (1:2, 1:1, and 2:1). From the results, when protein:MSN weight ratio increased, the percent entrapment efficiency of all MSNs decreased but the total amount of loaded protein increased.

The effect of pH on protein adsorption/interaction with different surface-charged MSNs was studied by measuring the ζ-potential of non-labeled nanoparticles and FITC-BSA as well as percent loading capacity and entrapment efficiency of FITC-BSA at different pHs (4, 5, and 6) (Figure S1). The isoelectric point (IEP), which describes the pH value at which electrokinetic movement of the particle/protein is zero, was determined for FITC-BSA and differently surface-modified MSNs. Using pH lower

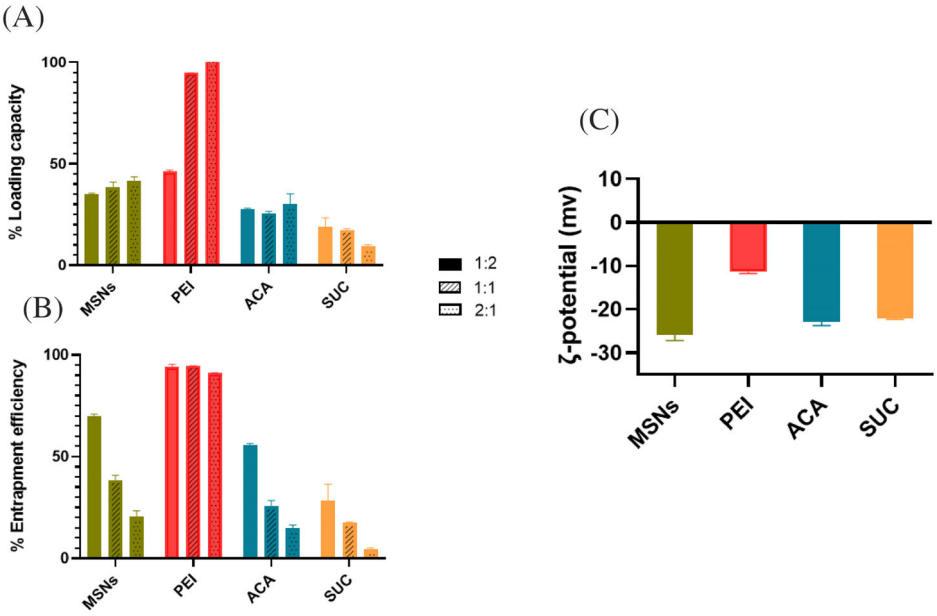

FIGURE 2 Protein loading trials at pH 5 in three different F-BSA:MSN weight ratios of 1:2, 1:1, and 2:1 (A) percent loading capacity and (B) percent entrapment efficiency. (C) Zeta potential values of protein-loaded nanoparticles using FITC-BSA:MSN weight ratio of 1:2 measured at pH 7.2.

than IEP, the protein/MSNs showed a positive ζ-potential while at pH higher than IEP, the protein/MSNs exhibited a negative ζ-potential (Figure S1a). Pristine MSNs, ACA-MSNs, and SUC-MSNs showed IEPs at 4, 6, and 5, respectively. PEI-MSNs displayed a positive charge with no IEP detected within the entire studied pH range, which contributed to the protonation of amino groups on the surface, and resulted in shifting the IEP to a higher value of around 10.6.[51] According to the measurements, the IEP of FITC-BSA at pH 5 can be considered the most suitable pH for protein loading.[52] At this pH, there is less repulsion between protein molecules, which promotes adsorption onto the silica surface.[53] This was confirmed by measuring the percent loading capacity and percent entrapment efficiency of FITC-BSA at pH 4, 5, and 6. As can be seen from Figure S1b-S1c, almost all nanoparticles reached the maximum loading capacity at pH 5, whereas less loading was observed at pH 4 and 6 regardless of surface modification. At pH 5, pristine MSNs and ACA-MSNs showed protein entrapment efficiency of around 70% and 55%, respectively. PEI-MSNs showed the highest entrapment efficiency of around 90% at pH 5 and 6, which is related to electrostatic interactions between the positively charged PEI-MSNs and the negatively charged FITC-BSA at higher pH. On the other hand, SUC-MSNs showed the least entrapment efficiency compared with other MSNs, which might be attributed to charge similarity with FITC-BSA within the studied pH range. Accordingly, pH 5 with the weight ratio of protein:MSN at 1:2 was chosen as the optimal loading condition for all MSNs.

Subsequently, the effect of protein loading on the nanoparticles' net surface charge was studied by comparing the ζ-potential values of all MSNs before and after protein loading (Figures 1C and 2C). Based on the ζ-potential analysis, the protein loading into MSNs altered the net surface charge, due to the negatively charged BSA protein.[54] Pristine MSNs (−29 mV) remained negatively charged with a net surface charge of −26 mV, whereas positively charged PEI-MSNs (+ 41 mV) became neutral with a net surface charge of −11 mV. BSA loading resulted in an increased negative net charge for ACA-MSNs from −14 mV to −23 mV, whereas it decreased the negative net charge of SUC-MSNs from −36 mV to −22 mV. The decrease in the ζ-potential of SUC-MSNs could be explained by the occurrence of adsorbed proteins on the surface of SUC-MSNs or electrostatic shielding of BSA reducing the effective surface charge.[55] The effect of protein loading on the net surface charge of the nanoparticles proposed that adsorption of FITC-BSA occurs both inside the mesopores of pristine MSNs and on the surface of PEI-MSNs, ACA-MSNs, and SUC-MSNs.

4.3 | Nanocomposite hydrogel formulation

As seen in **Table 1**, 1 wt% T-CNF and 2 wt% GGMMA were kept constant as the polymeric components throughout the ink formulations, but differently surface-charged non-loaded MSNs (MSNs, PEI-MSNs, ACA-MSNs, and

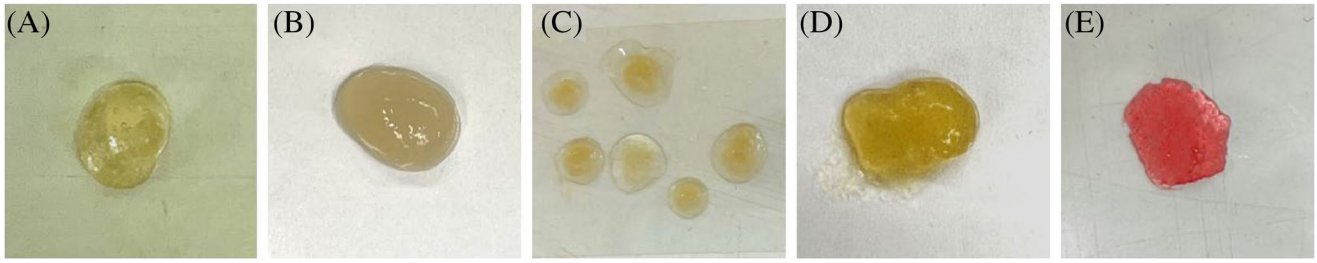

FIGURE 3 Photographic images show (A) plain hydrogel, (B) representative image of intact non-loaded nanocomposite hydrogel (MSNs, ACA-MSNs and SUC-MSNs), (C) phase-separated PEI-MSNs nanocomposite hydrogel, (D) representative image of 1 wt% protein-loaded nanocomposite hydrogel (MSNs, PEI-MSNs, ACA-MSNs and SUC-MSNs) and (E) representative image of 1 wt% protein-loaded TRITC-labeled nanocomposite hydrogels (MSNs, PEI-MSNs, ACA-MSNs and SUC-MSNs).

SUC-MSNs) in three different concentrations (0.5, 1, and 2.5 wt%) were mixed in the hydrogels. All MSNs (MSNs, ACA-MSNs, and SUC-MSNs) except PEI-MSNs were successfully incorporated into the hydrogel matrix in the three different concentrations and showed intact hydrogel matrices as the plain hydrogel (Figure 3A,B). Incorporation of PEI-MSNs led to phase separation (fibers aggregation) from concentrations of 0.5 wt% upwards (Figure 3C). All protein-loaded nanoparticles of concentration 1 wt% (MSNs, PEI-MSNs, ACA-MSNs and SUC-MSNs), both non-labeled and TRITC-labeled, yielded homogenous nanocomposite hydrogel matrices without phase separation (Figure 3D,E).

4.4 | Rheological assessments on MSN-laden hydrogels

The rheological properties of the hydrogel are important to assess before subjecting the material system to extrusion-based and semi-solid 3D printing.[7] Important rheological parameters in this context refer to viscosity and flow behavior, viscoelastic properties, and gel recovery behavior. Appropriate mechanical properties of the ink materials are sought after such as shear-thinning response to facilitate ink extrusion out of the needle with minimal shear stress and free of clogging, high zero-shear viscosity (viscosity during rest), and fast shear recovery properties, aiming to achieve high printability and printing fidelity.

Preliminary trials were conducted by mixing differently surface-charged non-loaded MSNs in three different concentrations (0.5, 1, and 2.5 wt%) with the polymeric matrix to understand the physical interaction between different surface-charged MSNs and negatively charged T-CNF as well as to determine the MSNs concentration that would retain a suitable viscoelastic property after their incorporation within the hydrogel. Then, this suitable MSNs concentration was used to formulate protein-loaded nanocomposite hydrogels, which their rheological behaviors were reassessed after that.

4.4.1 | Viscosity and flow behavior

Viscosity is the resistance of fluid to flow under stress. It can be used as criteria to correlate the ink performance during printing.[20] In our study, the viscosity of the formulated inks mainly originates from T-CNF, which can form a stable hydrogel by fibril-fibril entanglement and strong repulsion between nanofibrils due to the presence of negatively charged carboxylate groups. Non-charged biomacromolecule of GGMMA can strongly adsorb on the fibril surface of T-CNF via hydrogen bonding.[16] Because the negative charge on the surface of T-CNFs is sensitive to the presence of other charged surfaces in the ink formulation, four different MSNs (MSNs, PEI-MSNs, ACA-MSNs, and SUC-MSNs) with three different concentrations (0.5, 1, and 2.5 wt%) were tested. From Figure 3, it was found that all MSNs were successfully incorporated into the hydrogel matrix except for PEI-MSNs (Figure 3C). Although PEI-MSNs showed phase separation, the viscosity and flow behavior of 0.5 and 1 wt% PEI-MSNs particles were presented to elucidate the particle-matrix interactions.

Figure S2 describes the effect of different surface-charged particles and their concentrations on the hydrogel viscosity. According to the power law equation (Equation 3), the power law index (n) was calculated to describe the shear-thinning behavior of the hydrogels. The plain hydrogel and all nanocomposite hydrogels showed good shear-thinning properties with a power law index equal to or less than 0.27 (see Figure S2a and Table S1). In addition, the consistency index was compared through the sample series as the viscosity values at shear rate $1s^{-1}$. It was observed that increasing pristine MSNs (with hydroxyl groups) and ACA-MSNs (with neutral acetyl groups) concentrations resulted in increasing nanocomposite hydrogel consistency index without affecting zero shear viscosity

plateau (Figure S2a-S2b). Increasing PEI-MSNs concentration not only increased the consistency index but also prolonged the zero-shear viscosity plateau. In contrast, increasing SUC-MSNs concentration up to 1 wt% showed less change in the zero-shear viscosity compared to plain hydrogel with shortening in the zero-shear viscosity plateau. We then speculate that MSNs and ACA-MSNs surface charge has less effect on the repulsion between the fibers and interactions such as hydrogen bonds between the fibers and the nanoparticles may contribute to increasing the viscosity. For PEI-MSNs, phase separation is due to the screening of the negative charge of the nanofibrils by the positive charge (amino groups) on the surface of the PEI-MSNs, which induces the fiber flocculation and loss of homogenous fiber network in the gel structure.[56] On the contrary, SUC-MSNs (carboxylic groups) resulted in increasing the electrostatic repulsion between the nanofibrils and decreasing the propensity of aggregation.

4.4.2 | Viscoelastic properties

LVER and gel strength were measured in amplitude sweep to characterize the viscoelastic properties of the nanocomposite hydrogels. In addition, FTI was quantified based on the oscillatory measurements as a metric indicative of how much stress is needed for the transition from gel to sol.

Figure 4A,B shows the viscoelastic moduli (storage modulus G' and loss modulus G'') measured in the amplitude sweep as a function of shear strain and shear stress, respectively. Figure 4C–E gives a visual depiction of LVER, gel strength, and FTI of the different MSNs in different concentrations, respectively. According to Figure 4C, increasing pristine MSNs concentration to 1 wt% resulted in increasing in the LVER compared to the plain hydrogel. Although the incorporation of 0.5 wt% ACA-MSNs increased the LVER, a further increase in the particle concentrations resulted in a decrease in the LVER. The incorporation of 1 wt% SUC-MSNs in the hydrogel exhibited less change in the LVER compared to the plain hydrogel but a decrease in elasticity was seen at a concentration of 2.5 wt%. As a concluding remark, the incorporation of 2.5 wt% particles regardless of the surface charge would result in decreasing the hydrogel elasticity as the particles disrupt the connected network of the polymeric matrix. Generally, for all MSNs, increasing the particle concentration to 1 wt% resulted in increasing the gel strength without affecting the FTI compared to plain hydrogel, but further increase in the particle concentration resulted in increasing both the gel strength and the FTI as more stress was needed to flow the hydrogel (Figure 4D,E).

Finally, a thixotropy or time-dependent test was deployed to evaluate the breakdown and build-up rate of the gel network during extrusion as well as to characterize the ability of the ink to restore its elasticity upon removal of straining. Rapid recovery of the hydrogel is critical to warrant rapid building of soft matter layer by layer in extrusion-based 3D printing. This can be estimated by determining the recovery percentage of the storage modulus (G') of the hydrogel after straining. As can be seen from Figure S3, increasing particle concentration to 1 wt% showed less effects on the percent recovery after applying a shear strain of 10% at 1.6 Hz for 10 seconds. However, further increase in the particle concentration resulted in a decrease in the percent recovery, most likely due to disturbance to the polymeric network in large volume fraction of particles. In conclusion, 1 wt% particle concentration was chosen as the suitable percentage for protein-loaded MSNs.

The effect of protein and protein-loaded nanoparticles on the hydrogel matrix was studied. Figure 5 represents the rheological properties of the plain hydrogel, 0.5 wt% FITC-BSA-loaded hydrogel, and 1 wt% FITC-BSA-loaded nanocomposite hydrogels. Figure 5A,B represent the flow behavior and consistency index graphs, respectively. Compared to non-loaded nanocomposite hydrogels, the incorporation of protein-loaded nanoparticles in the hydrogel showed less change in the viscosity in the case of pristine MSNs and ACA-MSNs. Remarkably, protein-loaded PEI-MSNs exhibited a nearly neutral charge (see Figure 2C), which then became compatible with the hydrogel and formed homogenous nanocomposite hydrogel without phase separation compared to 1 wt% non-loaded PEI-MSNs nanocomposite hydrogel. The consistency index of protein-loaded SUC-MSNs nanocomposite hydrogel showed a slight increase, which may be due to a decrease in the negative charge compared to the non-loaded one.

Figure 5C,D demonstrate the amplitude sweep test as a function of shear strain and shear stress, respectively. As can be seen from Figure 5E–G, protein-loaded MSNs, and ACA-MSNs showed no change in the gel strength compared to non-loaded particles, whereas protein-loaded SUC-MSNs showed a slight increase in the gel strength. In all particles except PEI-MSNs, there is a slight drop in LVER and a slight increase in the FTI of protein-loaded particles compared to non-loaded ones. Compared to plain hydrogel and other nanoparticles, the incorporation of protein-loaded PEI-MSNs in the hydrogel matrix resulted in increasing the gel strength, decreasing viscoelasticity, and increasing the FTI (more stress needed to flow). Protein-loaded nanoparticles showed more decrease in the hydrogel percent recovery compared to non-loaded nanoparticles (Figure 5H,I). It is worth mentioning that incorporating 0.5 wt% BSA into the matrix gave rheological behavior similar to protein-loaded MSNs and ACA-MSNs.

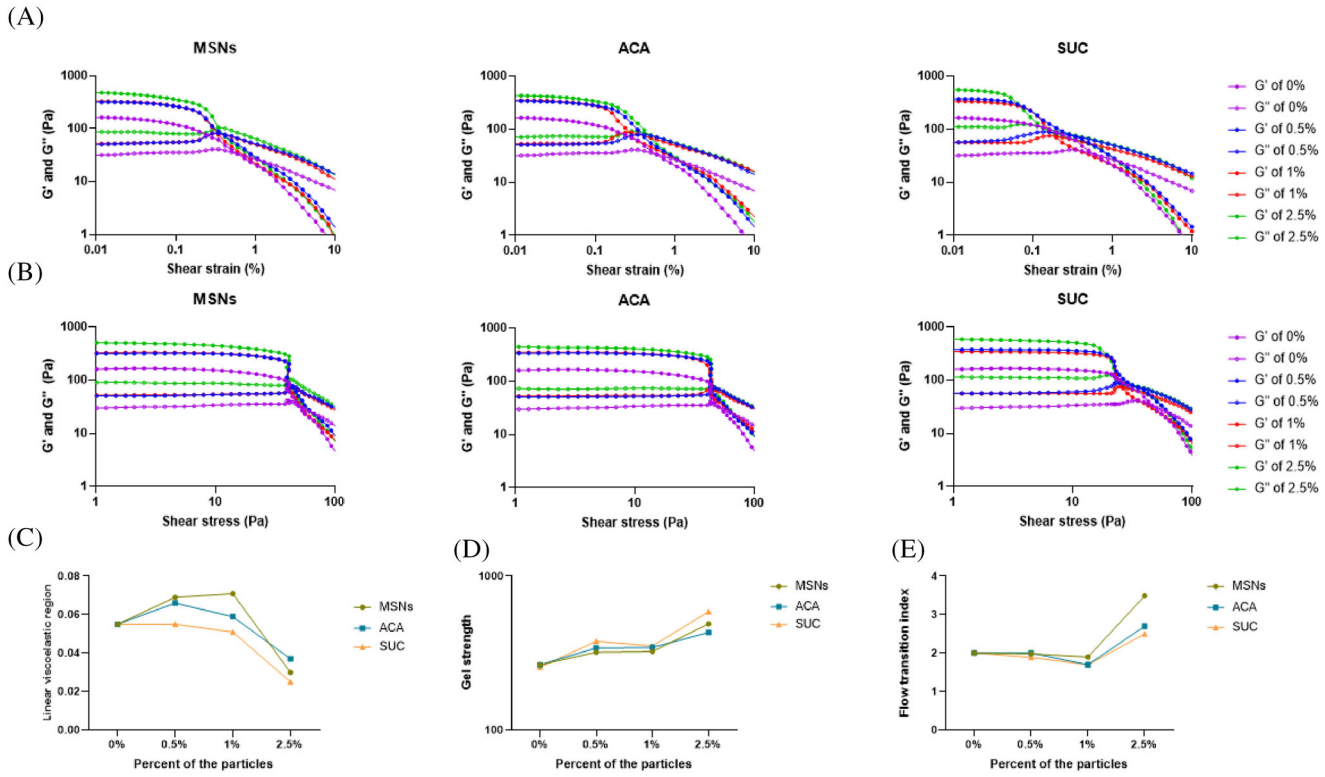

FIGURE 4 Viscoelastic moduli (G' and G") of non-loaded nanocomposite hydrogels (MSNs, ACA-MSNs and SUC-MSNs) in different concentrations (0, 0.5, 1, and 2.5 wt%) as a function of (A) shear strain and (B) shear stress. C, The linear viscoelastic region, LVER), (D) gel strength, and (E) flow transition index (FTI) are obtained from amplitude sweep graphs. LVER, The linear viscoelastic region; FTI, flow transition index.

In conclusion, compared to non-loaded particles, protein loading does not significantly change the rheological properties of the nanocomposite hydrogels except for PEI-MSNs. Previously, cationic-modified silica nanoparticles were seen to enhance the mechanical strength of the hydrogel of an anionic polymer matrix (alginate and gellan gum) by electrostatic interactions.[38] In our study, the incorporation of plain PEI-MSNs into T-CNF/GGMMA induced phase separation, but the protein loading in PEI-MSNs altered the surface charge of the nanoparticle with a change from +40 to −11 mV before and after BSA loading, which eventually facilitates the compatibility of protein-loaded cationic-modified MSNs with the anionic T-CNF in the nanocomposite ink formulation.

4.5 | Printability assessment

Besides rheology as a method to evaluate the printability, a semiquantitative method was developed by Ouyang et al.[57] based on which printability index (Pr) can be calculated for square shape from Equation (4) via image analysis (perimeter and area determination). The printability index is a useful parameter to show the difference between the predesigned structure and the printed one. Figure 6A–C depicts the photographic images of the printed two layers and corresponding microscopic images of the intersection and pore shape. Figure 6D shows Pr values that were calculated from image analysis. It was observed that all prepared inks showed Pr values in the range of 0.85–0.89, which indicates under-gelation conditions with less difference between plain and protein-loaded nanocomposite structures. It was referred that inks showed good printability when Pr values range between 0.9 and 1.1.[58] Figure 6E,F shows the representative photographic images of the four-layered 3D printed scaffolds used in the following study.

4.6 | Release study

4.6.1 | In vitro protein release study

FITC-BSA release was evaluated from 3D printed hydrogels, different 3D printed nanocomposite structures as well as MSN without matrix to study the effect of MSNs, the net surface charge of MSNs, and matrix on controlling protein release (Figure 7). From Figure 7A, FITC-BSA showed burst release (around 80% in 30 minutes and almost 100%

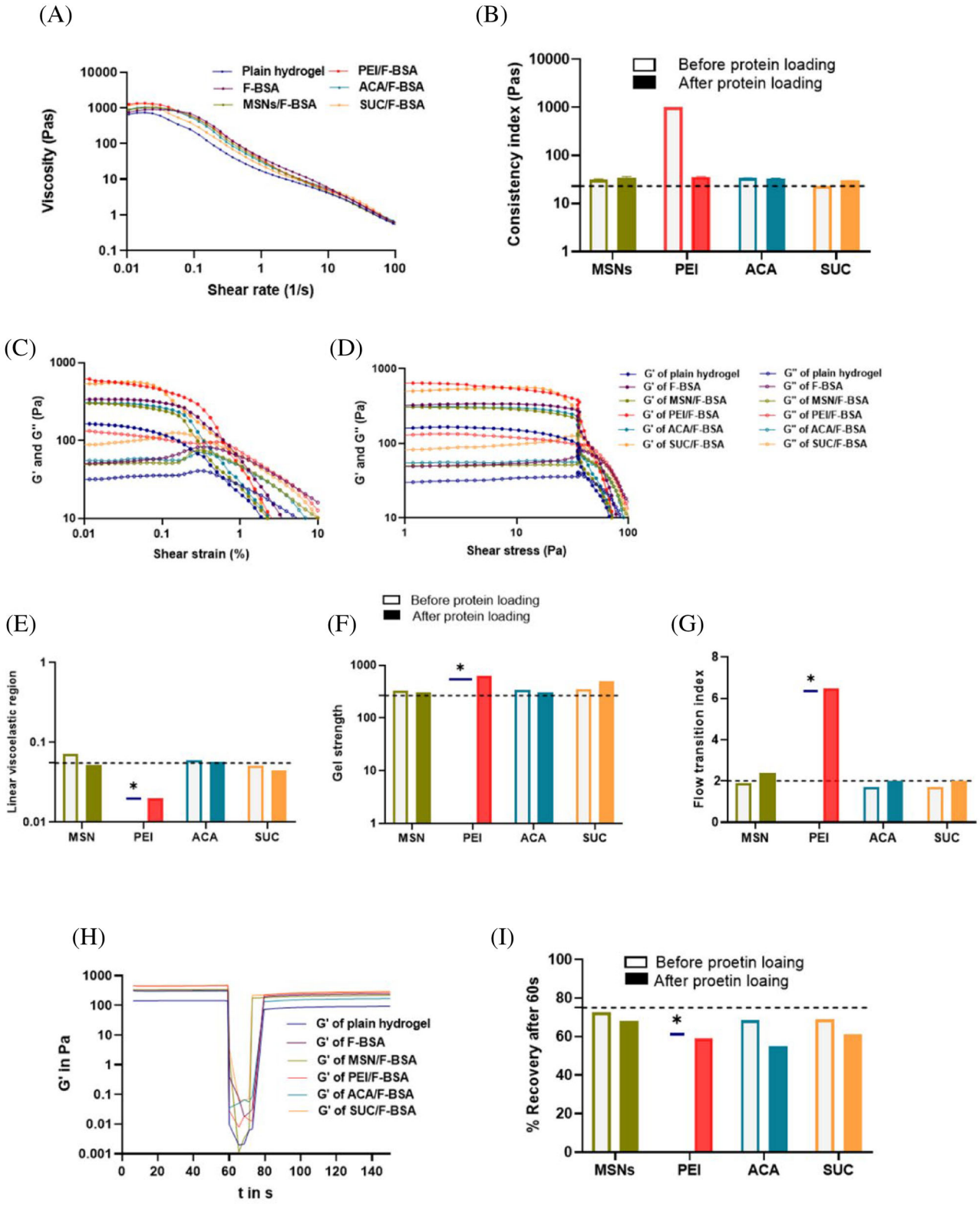

FIGURE 5 Rheological evaluation of different formulations. (A) The flow behavior of plain hydrogel, 0.5 wt% FITC-BSA-loaded hydrogel, and 1 wt% FITC-BSA-loaded nanocomposite hydrogels and (B) consistency index of nanocomposite hydrogels before and after protein loading. Viscoelastic moduli (G' and G'') of plain hydrogel, 0.5 wt% FITC-BSA-loaded hydrogel, and 1 wt% FITC-BSA-loaded nanocomposite hydrogels plotted against (C) shear strain and (D) shear stress. E, F, and G, Linear viscoelastic region (LVER), gel strength, and flow transition index (FTI) before and after protein loading, respectively. (H) Time-dependent of plain hydrogel, 0.5 wt% FITC-BSA-loaded hydrogel, and 1 wt% FITC-BSA-loaded nanocomposite hydrogels and (I) the percent recovery after 60 seconds before and after protein loading. The dotted lines represent the corresponding values of the plain hydrogel. * represents phase separation.

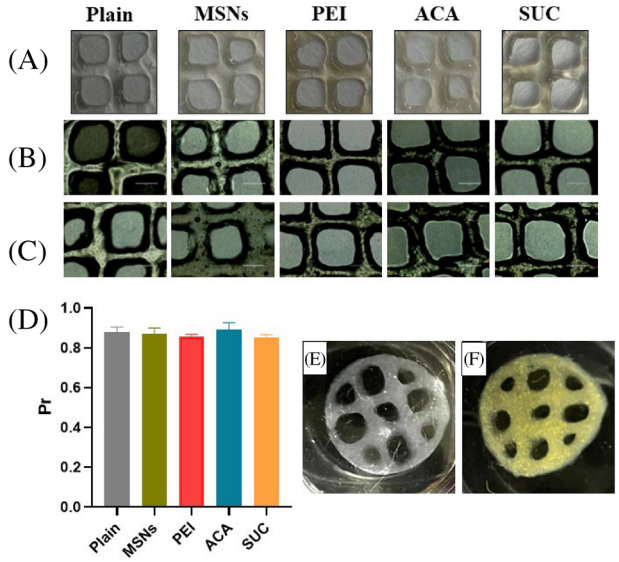

FIGURE 6 Printability assessment of plain and different protein-loaded nanocomposite biomaterial inks (A) photographic images, (B) intersection, (C) the pore shape, and (D) the printability index (Pr). Representative images of 3D printed scaffolds of (E) plain hydrogel and (F) protein-loaded nanocomposite hydrogel used in the release study. Pr, printability index.

release after 1 hour) from the 3D printed hydrogel, whereas more sustained release was observed from the different 3D printed nanocomposite structures. It was observed that the maximal release percentage of FITC-BSA from the 3D printed nanocomposite structures followed the order ACA-MSNs > SUC-MSNs > PEI-MSNs > MSNs with around 80%, 59%, 46%, and 15% protein released after 7 days, respectively. As discussed previously (Section 4.2), the presence of FITC-BSA inside mesopores accounts for slower release from pristine MSNs and faster release from the other MSNs. On the other hand, electrostatic interactions between FITC-BSA and PEI-MSNs can be responsible for slower release compared to ACA-MSNs and SUC-MSNs. Compared to Figure 7B, we found that protein release from protein-loaded nanoparticles followed the same order as 3D nanocomposite structures. The effect of the matrix on controlling the protein release was only observed from 3D printed PEI-MSNs nanocomposite structures with around 46% in 48 hours, whereas it reached around 43% in 30 minutes from protein-loaded MSNs. Hence, we conclude that protein release from different surface-charged MSNs is mainly dependent on protein location (adsorption inside the mesopores or on the surface) and interactions between the protein and particles' surface (net charge).

The in vitro protein release data was fitted by the Korsmeyer-Peppas model. The release power "n" values for the Korsmeyer-Peppas model were calculated according to Equation (5). It was found that FITC-BSA release from different 3D printed protein-loaded nanocomposite structures followed a diffusion-controlled mechanism (Fickian diffusion) with n values less than 0.5, while its release from the 3D printed hydrogel followed non-Fickian or anomalous diffusion mechanism (Table S2) according to this model. This difference in the release mechanisms can be connected to the presence of nanoparticles in the nanocomposite structures. In the 3D-printed hydrogel without particles, FITC-BSA release is controlled by both polymer relaxation and diffusion. However, the relaxation of the polymeric matrix in the 3D printed nanocomposite structures is restricted due to the presence of particles and possibly some degree of physical crosslinking between the particles and the matrix, which restricts the polymer relaxation hence, the release is governed only by diffusion.[59]

4.6.2 | Protein thermal stability study

The present study also investigated the thermal stability of proteins using intrinsic tryptophan fluorescence (ITF) at 330 and 350 nm as a measure of protein unfolding at increasing temperatures. Specifically, Nano differential scanning fluorimetry (NanoDSF) was utilized as a reliable and simple tool for this purpose.[42] The tryptophan residue, located in the hydrophobic core of proteins, emits intrinsic fluorescence when exposed to the external environment due to temperature increase. This emission can be measured at 330 and 350 nm wavelengths depending on the nature of the external environment. In an apolar environment, the tryptophan fluorescence emission maximum is at 330 nm. However, when the environment becomes polar, the intensity of tryptophan emission decreases due to static and dynamic quenching by solvent molecules, and the peak emission is red shifted to a higher wavelength of 350 nm. Red shifting is generally observed for proteins that have tryptophan in the hydrophobic core and are exposed to aqueous solvents. However, some proteins exhibit a blue shift when tryptophan is on the surface or from interior tyrosine residues.[60]

Figure S4 displays the first derivative results of the (F350/F330) ratio plotted as a function of temperature for FITC-BSA/PBS as a reference and different release media at various time points. The control experiment, where FITC-BSA was dissolved in PBS buffer, revealed a blue shift with a melting peak observed at 60°C, consistent with the previously reported melting peak of BSA at 64°C.[61] In contrast, all protein samples detected after release exhibited a red shift, which may be due to changes in the external environment resulting from the release of

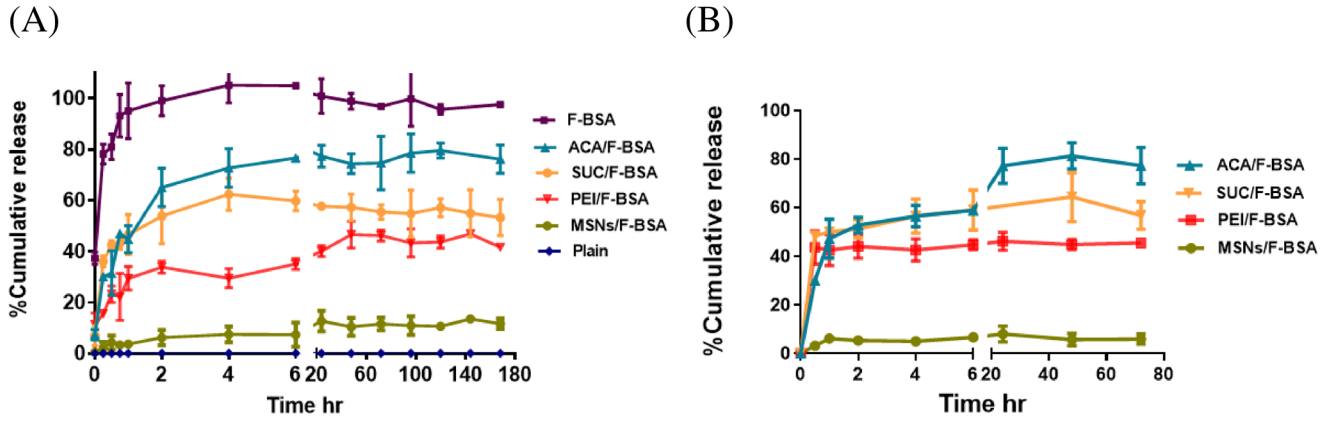

FIGURE 7 Cumulative percent release of FITC-BSA from (A) different 3D printed structures and (B) FITC-BSA-loaded nanoparticles.

some components from the printed structures that quench the fluorescence emission at 330 nm and shift to 350 nm. This was confirmed by measuring the release sample from the plain matrix, where a peak was detected, which could interfere with the measurements. Concerning protein release from the 3D printed structures, we observed that the FITC-BSA melting peaks were detected at 74°C, 66°C, and 67°C after 48 hours for FITC-BSA-loaded hydrogel, PEI-MSNs, and SUC-MSNs nanocomposite 3D printed structures, respectively, and the peak magnitudes increased with time, indicating protein release from the 3D printed structures. This shift in the melting temperature may be due to the matrix's effect on enhancing protein stability. However, for ACA-MSNs nanocomposite 3D printed structure, the melting temperature could not be detected clearly, and no protein melting peaks were detected in the release media of pristine MSNs nanocomposite 3D printed structure, indicating a small amount of protein release. These findings are consistent with the release study's results. Our findings thus confirm that the NanoDSF technique is a reliable method for determining protein stability through ITF measurements in ink formulation.

4.6.3 | Evaluation of nanoparticles and protein release by confocal microscopy and transmission electron microscopy

Taking advantage of easy labeling MSNs and BSA with fluorescent dyes, visualization of protein-loaded nanoparticles within the matrix can be carried out using confocal microscopy. This would be a valuable and quick method to assess nanoparticle distribution within the matrix and to confirm protein release. To detect particle distribution within the 3D printed structures, low MSNs concentration (0.1 wt%) was used in the nanocomposite matrix. Microscopic images of different 3D printed FITC-BSA-loaded TRITC-nanocomposite structures are depicted in Figure 8A. Based on our observations, all protein-loaded MSNs distributed homogenously within the matrix without significant differences among various types of MSNs, which proves that protein-loaded MSNs can be utilized to formulate a homogenous nanocomposite. In addition, FITC-BSA release from different 3D printed nanocomposite structures was evaluated using confocal microscopy with MSNs concentration of 1 wt%. Figure S5 showed the microscopic images of different 3D printed protein-loaded structures before and after 7 days of release. Parallel with the in vitro release results, MSNs nanocomposite structure showed less FITC-BSA release, whereas more FITC-BSA release was observed from 3D printed hydrogel as well as PEI-MSNs, ACA-MSNs, and SUC-MSNs nanocomposite structures.

Nanoparticle diffusion from the 3D printed nanocomposites and their degradation behavior during the release process was determined using TEM at two time points, after 24 hours and 7 days. Figure 8B shows TEM images obtained from the release medium of different 3D printed nanocomposite structures. Particle size distribution was analyzed, and the results are depicted in Figure S6. In these figures, all different MSNs were detected in the release media with the most obvious particle degradation in the case of pristine MSNs. This can be explained by hydrolysis of the silica matrix under aqueous conditions due to the hydrolytic breakdown of the siloxane bonds (Si-O-Si), which results in morphological changes of the MSNs accompanied by loss of the mesoporous structure. Although PEI-MSNs showed less change in particle size, there was a complete absence of the mesoporous structure after 7 days. The absence of the mesopores particularly for this sample could be explained by the basic local buffering effect of PEI, which leads to a faster hydrolysis rate whereas the positive charge of PEI enhances the redeposition of the dissolved negative silicic acid species onto the surface of the nanoparticles.[62]

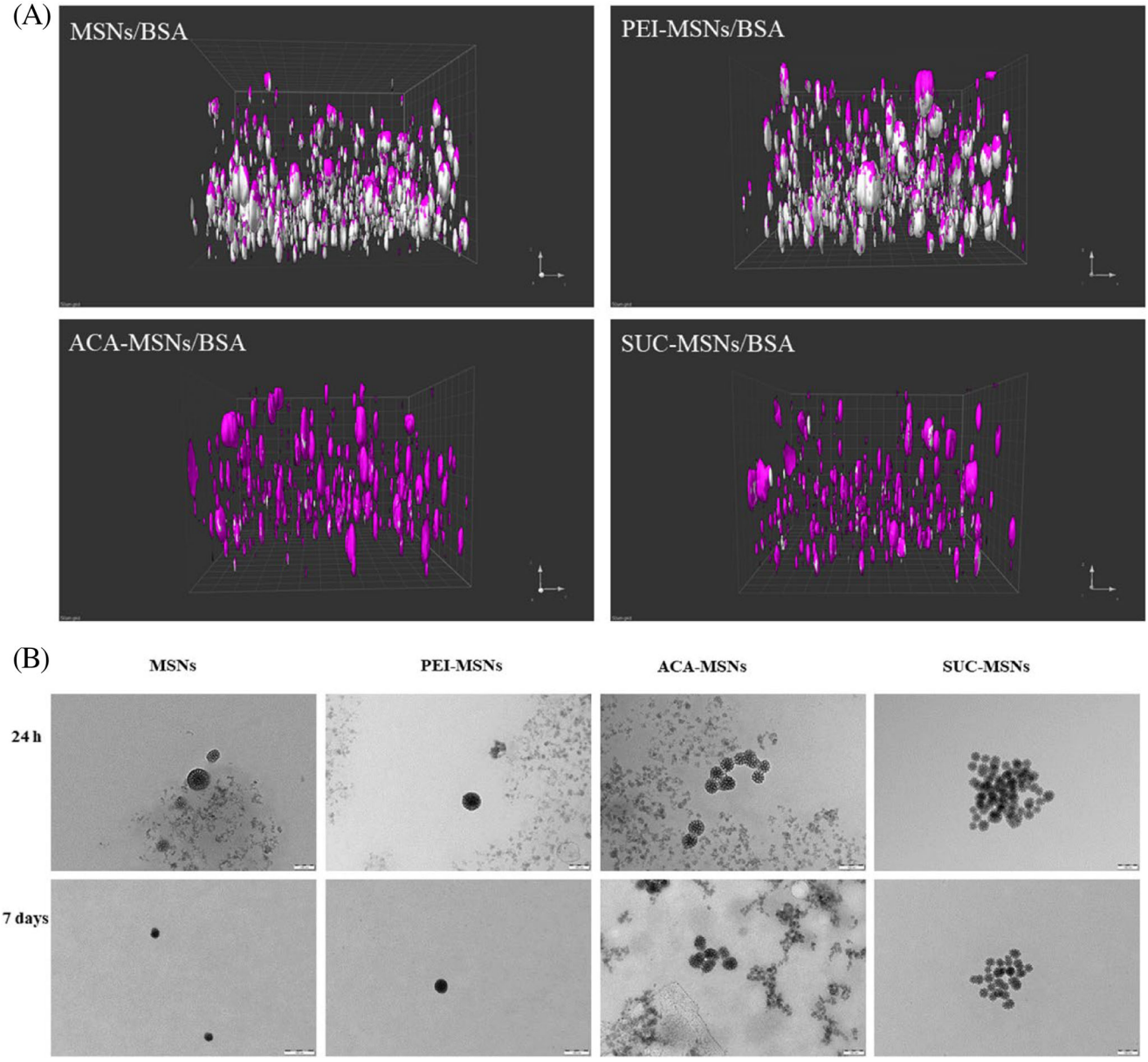

FIGURE 8 Nanoparticles distribution and release from nanocomposite matrices evaluated using confocal and transmission electron microscopy. (A) Different protein-loaded mesoporous silica nanoparticles' distribution within the 3D printed structures before release (MSN concentration 0.1 wt%) obtained using confocal microscopy. Composite images consist of overlayed FITC-BSA (white) and TRITC-MSNs (magenta) in the matrix. (B) TEM images of the release media of different 3D printed nanocomposite structures after 24 hours and 7 days. Scale bar 100 nm.

5 | CONCLUSION

We have successfully demonstrated the effect of differently surface-charged MSNs on protein loading as well as on the colloidal stability and printability of hybrid nanocomposite hydrogels based on the incorporation of these with anionic cellulose nanofibers (T-CNF). PEI-MSNs showed maximum protein entrapment efficiency compared to the others with net surface charge reversal from highly positive to neutral charge after loading of the protein with net negative charge at formulation conditions. The effective surface charge of MSNs clearly plays a key role in dictating the particle-matrix interactions in the formulated biomaterial ink. Without loading any protein, neutral or negatively net-charged MSNs were compatible with the polymeric matrix of T-CNF and GGMMA, without affecting the colloidal stability of T-CNF. With the FITC-BSA protein loaded into MSNs, all four types of MSNs were found suitable to be incorporated with this xeno-free hydrogel of T-CNF/GGMMA, with appropriate rheological properties to render very decent printability of the developed biomaterial inks. Intriguingly, although

phase separation was observed when the highly positively charged PEI-MSNs was mixed into the hydrogel, the FITC-BSA loaded PEI-MSNs could be successfully incorporated within the matrix. The release of FITC-BSA was dependent on the particle-matrix interactions as well as the type of surface-charged MSNs. In conclusion, the MSN-incorporated nanocomposite biomaterial inks could be considered as a promising hydrogel platform for the delivery of biologics in 3D.

ACKNOWLEDGMENTS

Imaging/Flow cytometry was performed at the Cell Imaging and Cytometry Core, Turku Bioscience Centre, Turku, Finland, with the support of Biocenter Finland. Transmission electron microscopic samples were carried out in the Electron Microscopy Laboratory, Institute of Biomedicine, University of Turku, and Biocenter Finland. A.M. would like to acknowledge the financial support from the Ministry of Higher Education of the Arab Republic of Egypt. European Regional Development Fund (ERDF) REACT EU (Centre for Additive Manufacturing for Life Science and Pharmaceutical Industry, project code A77805, E.Ö., C.X., J.M.R.), Sigrid Jusélius Foundation (J.M.R), Academy of Finland (333158, X.W., Q.B.), Swedish Cultural Foundation (E.Ö.) and Magnus Ehrnrooth Foundation (E.Ö.) are acknowledged for financial support. Rathna Mathiyalagan is gratefully acknowledged for her assistance in rheology and 3D printing.

CONFLICT OF INTEREST STATEMENT

The authors declare no conflicts of interest.

DATA AVAILABILITY STATEMENT

The data that support the findings of this study are available in the supplementary material of this article.

REFERENCES

1. R. C. Advincula, J. R. C. Dizon, E. B. Caldona, R. A. Viers, F. D. C. Siacor, R. D. Maalihan, A. H. Espera, *MRS Commun.* **2021**, *11*, 539.
2. I. I. Andreadis, C. I. Gioumouxouzis, G. K. Eleftheriadis, D. G. Fatouros, *Pharmaceutics* **2022**, *14*, 609.
3. Y. Zhu, D. Joralmon, W. Shan, Y. Chen, J. Rong, H. Zhao, S. Xiao, X. Li, *Biodes Manuf* **2021**, *4*, 405.
4. J. Li, C. Wu, P. K. Chu, M. Gelinsky, *Mater. Sci. Eng. R Rep* **2020**, *140*, 100543.
5. M. V. Varma, B. Kandasubramanian, S. M. Ibrahim, *Mater Chem Phys* **2020**, *255*, 123642.
6. H. Bhuskute, P. Shende, B. Prabhakar, *AAPS PharmSciTech* **2022**, *23*, 1.
7. H. Li, C. Tan, L. Li, *Mater. Des.* **2018**, *159*, 20.
8. A. Indurkar, A. Pandit, R. Jain, P. Dandekar, *Int. J. Bioprint.* **2021**, *21*, e00127.
9. A. Saddique, I. W. Cheong, *Korean J Chem Eng* **2021**, *38*, 2171.
10. G. Chinga-Carrasco, *Biomacromolecules* **2018**, *19*, 701.
11. H. Paukkonen, M. Kunnari, P. Laurén, T. Hakkarainen, V.-V. Auvinen, T. Oksanen, R. Koivuniemi, M. Yliperttula, T. Laaksonen, *Int J Pharm* **2017**, *532*, 269.
12. S. S. Athukoralalage, R. Balu, N. K. Dutta, N. Roy Choudhury, *Polymers* **2019**, *11*, 898.
13. R. Weishaupt, G. Siqueira, M. Schubert, P. Tingaut, K. Maniura-Weber, T. Zimmermann, L. Thöny-Meyer, G. Faccio, J. Ihssen, *Biomacromolecules* **2015**, *16*, 3640.
14. W. Xu, B. Z. Molino, F. Cheng, P. J. Molino, Z. Yue, D. Su, X. Wang, S. Willfor, C. Xu, G. G. Wallace, *ACS Appl. Mater. Interfaces* **2019**, *11*, 8838.
15. J. Leppiniemi, P. Lahtinen, A. Paajanen, R. Mahlberg, S. Metsä-Kortelainen, T. Pinomaa, H. Pajari, I. Vikholm-Lundin, P. Pursula, V. P Hytönen, *ACS Appl. Mater. Interfaces* **2017**, *9*, 21959.
16. W. Xu, X. Zhang, P. Yang, O. Långvik, X. Wang, Y. Zhang, F. Cheng, M. Österberg, S. Willför, C. Xu, *ACS Appl. Mater. Interfaces* **2019**, *11*, 12389.
17. Q. Wang, O. Backman, M. Nuopponen, C. Xu, X. Wang, *Front Chem Eng* **2021**, *3*, 723429.
18. A. Chakraborty, A. Roy, S. P. Ravi, A. Paul, *Biomater Sci* **2021**, *9*, 6337.
19. A. K. Gaharwar, N. A. Peppas, A. Khademhosseini, *Biotechnol Bioeng* **2014**, *111*, 441.
20. F. Gao, C. Ruan, W. Liu, *Mater Chem Front* **2019**, *3*, 1736.
21. H. Fukuzumi, R. Tanaka, T. Saito, A. Isogai, *Cellulose* **2014**, *21*, 1553.
22. E. Barrett-Catton, M. L. Ross, P. Asuri, *Polymers* **2021**, *13*, 856.
23. M. Manzano, M. Vallet-Regí, *Adv Funct Mater* **2020**, *30*, 1902634.
24. A. Watermann, J. Brieger, *Nanomaterials* **2017**, *7*, 189.
25. S. Hosseinpour, L. J. Walsh, C. Xu, *J Mater Chem B* **2020**, *8*, 9863.
26. D. S. Karaman, D. Desai, R. Senthilkumar, E. M. Johansson, N. Råtts, M. Odén, J. E. Eriksson, C. Sahlgren, D. M. Toivola, J. M. Rosenholm, *Nanoscale Res Lett* **2012**, *7*, 1.
27. S. Rahmani, J. Budimir, M. Sejalon, M. Daurat, D. Aggad, E. Vives, L. Raehm, M. Garcia, L. Lichon, M. Gary-Bobo, *Molecules* **2019**, *24*, 332.
28. T. Xia, M. Kovochich, M. Liong, H. Meng, S. Kabehie, S. George, J. I. Zink, A. E. Nel, *ACS Nano* **2009**, *3*, 3273.
29. K.-C. Kao, T.-S. Lin, C.-Y. Mou, *J Phys Chem* **2014**, *118*, 6734.
30. D. Saikia, J. R. Deka, C.-E. Wu, Y.-C. Yang, H.-M. Kao, *Mater. Sci. Eng. C* **2019**, *94*, 344.
31. D. Kwon, B. G. Cha, Y. Cho, J. Min, E.-B. Park, S.-J. Kang, J. Kim, *Nano Lett* **2017**, *17*, 2747.
32. C. Xu, Y. He, Z. Li, Y. A. Nor, Q. Ye, *J Mater Chem B* **2018**, *6*, 1899.
33. J. Tu, A. L. Boyle, H. Friedrich, P. H. Bomans, J. Bussmann, N. A. Sommerdijk, W. Jiskoot, A. Kros, *ACS Appl. Mater. Interfaces* **2016**, *8*, 32211.
34. A. Zengin, J. Castro, P. Habibovic, S. Van Rijt, *Nanoscale* **2021**, *13*, 1144.
35. E. Piantanida, I. Boškoski, G. Quero, C. Gallo, Y. Zhang, C. Fiorillo, V. Arena, G. Costamagna, S. Perretta, L. De Cola, *Mater Today Bio* **2021**, *10*, 100109.
36. M. Zhu, Y. Zhu, L. Zhang, J. Shi, *Sci Technol Adv Mater* **2013**, *14*, 045005.
37. M. T. Tavares, V. M. Gaspar, M. V. Monteiro, J. P. S. Farinha, C. Baleizão, J. F. Mano, *Biofabrication* **2021**, *13*, 035012.
38. M. Lee, K. Bae, P. Guillon, J. Chang, Ø. Arlov, M. Zenobi-Wong, *ACS Appl. Mater. Interfaces* **2018**, *10*, 37820.

39. V. Nairi, S. Medda, M. Piludu, M. F. Casula, M. Vallet Regí, M. Monduzzi, A. Salis, *J. Chem. Eng.* **2018**, *12*, 50.
40. M. K. Jaiswal, J. R. Xavier, J. K. Carrow, P. Desai, D. Alge, A. K. Gaharwar, *ACS Nano* **2016**, *10*, 246.
41. C. Dannert, B. T. Stokke, R. S. Dias, *Polymers* **2019**, *11*, 275.
42. S. Lisina, W. Inam, M. Huhtala, F. Howaili, H. Zhang, J. M. Rosenholm, *Pharmaceutics* **2023**, *15*, 1473.
43. D. Shen, J. Yang, X. Li, L. Zhou, R. Zhang, W. Li, L. Chen, R. Wang, F. Zhang, D. Zhao, *Nano Lett* **2014**, *14*, 923.
44. D. Desai, D. S. Karaman, N. Prabhakar, S. Tadayon, A. Duchanoy, D. M. Toivola, S. Rajput, T. Näreoja, J. M. Rosenholm, *Open Material Sciences* **2014**, *1*.
45. J. M. Rosenholm, A. Penninkangas, M. Lindén, *Chem Commun* **2006**, 3909.
46. J. M. Rosenholm, A. Duchanoy, M. Lindén, *Chem Mater* **2008**, *20*, 1126.
47. D. Patra, D. Ş. Karaman, D. Desai, E. El Khoury, J. M. Rosenholm, *Mater Res Bull* **2016**, *84*, 267.
48. A. K. Meka, P. L. Abbaraju, H. Song, C. Xu, J. Zhang, H. Zhang, M. Yu, C. Yu, *Small* **2016**, *12*, 5169.
49. P. L. Ritger, N. A. Peppas, *J. Controlled Release* **1987**, *5*, 37.
50. B. Küçüktürkmen, W. Inam, F. Howaili, M. Gouda, N. Prabhakar, H. Zhang, J. M. Rosenholm, *Biosensors* **2022**, *12*, 181.
51. J. M. Rosenholm, M. Lindén, *Chem Mater* **2007**, *19*, 5023.
52. H. Shi, S. Liu, J. Cheng, S. Yuan, Y. Yang, T. Fang, K. Cao, K. Wei, Q. Zhang, Y. Liu, *ACS Appl. Mater. Interfaces* **2019**, *11*, 3645.
53. L.-C. Sang, A. Vinu, M.-O. Coppens, *Langmuir* **2011**, *27*, 13828.
54. D. Fologea, B. Ledden, D. S. McNabb, J. Li, *Appl Phys Lett* **2007**, *91*, 539011.
55. V. Nairi, S. Medda, M. Piludu, M. F. Casula, M. Vallet-Regì, M. Monduzzi, A. Salis, *Chem Eng J* **2018**, *340*, 42.
56. E. Saarikoski, T. Saarinen, J. Salmela, J. Seppälä, *Cellulose* **2012**, *19*, 647.
57. L. Ouyang, R. Yao, Y. Zhao, W. Sun, *Biofabrication* **2016**, *8*, 035020.
58. H. Jongprasitkul, S. Turunen, V. S. Parihar, M. Kellomäki, *Int. J. Bioprint.* **2022**, *25*, e00185.
59. T. M. S. Udeni Gunathilake, Y. C. Ching, C. H. Chuah, *Polymers* **2017**, *9*, 64.
60. A. Real-Hohn, M. Groznica, N. Löffler, D. Blaas, H. DSF Kowalski, *Front Microbiol* **2020**, *11*, 1442.
61. O. Matsarskaia, L. Bühl, C. Beck, M. Grimaldo, R. Schweins, F. Zhang, T. Seydel, F. Schreiber, *Phys Chem Chem Phys* **2020**, *22*, 18507.
62. E. von Haartman, D. Lindberg, N. Prabhakar, J. M. Rosenholm, *Eur J Pharm Sci* **2016**, *95*, 17.

SUPPORTING INFORMATION

Additional supporting information can be found online in the Supporting Information section at the end of this article.

How to cite this article: A. Mahran, E. Özliseli, Q. Wang, I. Özliseli, R. Bhadane, C. Xu, X. Wang, J. M. Rosenholm, *Nano Select*. **2023**, 1.
https://doi.org/10.1002/nano.202300097